

# Aerodynamic Behavior of Compliant Membranes as Related to Bat Flight

Rye M. Waldman<sup>1</sup>, Arnold J. Song<sup>1</sup>, Daniel K. Riskin<sup>2</sup>, Sharon M. Swartz<sup>3</sup>, and Kenneth S. Breuer<sup>4</sup>  
*Brown University, Providence, Rhode Island, 02912*

We present computations of membrane airfoil behavior subject to aerodynamic loading and compare them with *in vivo* measurements of membrane wings of bats during flight. The computational method assumes an inviscid potential flow (with net circulation determined by a Kutta condition), is computed using XFOIL and iteratively coupled with a finite element model describing the membrane behavior. We find that a simple model assuming uniform loading is largely confirmed, particularly for very compliant membranes in which the pressure loading is focused at the center of the airfoil. Stiffer wings transition to the more traditional pressure distribution predicted by thin airfoil theory for rigid wings. Comparisons with sail theories are also made, illustrating the effect of compliance. Additionally, the *in vivo* measurements of membrane deformation during bat flight are acquired from detailed kinematics recorded from *Cynopterus brachyotis*, flying in a wind tunnel. We demonstrate that the expansion of the wing area during the downstroke of the flight cycle exhibits area increases of up to 100% during the downstroke. In addition, comparisons with the computational theory show good qualitative agreement.

## Nomenclature

$A$	= element area
$A$	= membrane shape amplitude
$A_0$	= reference surface area
$\alpha$	= angle of attack
$C_L$	= lift coefficient
$C_p$	= coefficient of pressure, $2(P - P_0)/\rho U^2$
$c$	= chord
$\Delta C_p$	= differential coefficient of pressure
$\Delta P$	= pressure differential
$\Delta z$	= root-mean-square profile shape change
$\varepsilon$	= strain
$\varepsilon_0$	= pre-strain
$Fn$	= non-dimensional chord-normal aerodynamic loading
$i$	= nodal index
$L$	= lift force
$L$	= deformed membrane length
$L_0$	= unstressed membrane length
$N$	= number of membrane nodes
$Re$	= Reynolds number
$\rho$	= fluid density
$S$	= planform area
$T$	= membrane tension
$Tn$	= non-dimensional chord-normal component of membrane tension
$t$	= membrane thickness

<sup>1</sup> Ph.D. Candidate, Div. of Engineering, Box D, Brown University, Providence, RI 02912, Student AIAA

<sup>2</sup> Postdoctoral Researcher, Ecol. and Evol. Biology, Box G-B206, Brown University, Providence, RI 02912

<sup>3</sup> Associate Professor, Ecol. and Evol. Biology, Box G-B206, Brown University, Providence, RI 02912

<sup>4</sup> Professor, Div. of Engineering, Box D, Brown University, Providence, RI 02912, Senior Member AIAA

$U$	=	freestream velocity
$w$	=	relaxation constant
$x$	=	chord-wise position
$z$	=	membrane chord-normal deflection
$z_{\max}$	=	maximum camber

## I. Introduction

Recently, much research effort has gone into the design and flight characterization of micro-air vehicles (MAVs) [1]. Unfortunately, the scaling down of vehicle size is accompanied by a host of complications which apply to the flight of vehicles at these reduced size scales due to the amplification of the effects of complex flow phenomena at low to moderate Reynolds numbers ( $Re < 100k$ ). In this Reynolds number range, the diminutive scale of the vehicle is near that of the viscous flow features requiring more accurate prediction of flow separation, turbulent separation, and reattachment to properly characterize aerodynamic performance. Not only are these flow phenomena difficult to model, they are also extremely sensitive to perturbations already present in ambient flow which can significantly change results from case to case [2].

We, as do others, look to biology for inspiration in the design of low-Reynolds number flyers. Invertebrate, avian and mammalian flyers have already “solved” the problem of low-Reynolds number flight and are optimized for a variety of flight modes and flow conditions, from long-range soaring to hovering flight. For this paper, we focus on the unique aerodynamic structure of the bat wing, specifically the lesser dog-faced fruit bat, *Cynopterus brachyotis*. This species has an average body mass of 40 grams with wing dimensions of 40 cm (span) by 10 cm (average chord length). Typical flight speeds range from 2 to 10 m/s and these bats routinely exhibit extraordinary flight maneuverability by performing extremely small radius turns, perching and obstacle avoidance. In addition, these bats maintained a high level of flight performance despite large changes in wing loading. The unique wing structure of bats and other mammalian gliders are composed of a thin, compliant skin membrane which can deform quite considerably in flight and may be a key component in the remarkable flight capabilities of these animals.

The aeromechanics of compliant membrane wings has received considerable attention in the past few years, and a variety of studies have demonstrated that compliancy can significantly improve lift characteristics as a result of the adaptive increase in camber due to aerodynamic loading [3-8]. The stall behavior of these wings was also seen to be improved, i.e. the drop in lift at stall is made to be less severe and the wing exhibits a “gentle” drop in lift with increases in angle of attack.

A simple theory for the static behavior of these wings was presented by Song et al., [9] and is based on the behavior of a compliant membrane subject to uniform loading. Using this approach good agreement was found with wind tunnel experiments. The model, however, is quite crude and the object of our current research is to explore a more sophisticated model for the wing behavior.

In the current paper, we have two goals: Firstly we extend the simple theory of Song et al. [9] by using inviscid, potential flow aerodynamic methods coupled with the elastic behavior of the membrane-wing. Although this approach ignores critical issues associated with low Reynolds number aerodynamics (in particular, leading edge separation and re-attachment), it should exhibit an aeroelastic response appropriate for moderate wing loading, and furthermore, will help to elucidate how the uniform loading model of Song et al. was so successful, despite its simplicity. In the second portion of the paper, we present *in vivo* measurements of the compliance of the membranes in freely flying bats, and use these measurements to determine the extent of membrane deformation that occurs during biological flight. These two topics – the numerical modeling and the *in vivo* measurements – although closely related, are quite distinct. The next two sections (II and III) discuss the methods and results of numerical simulations of membrane wings and represent the natural extension of the uniform-loading theory. Sections IV and V present the methods and results of our *in vivo* study of bat wing membranes during flight.

## II. Simulation Method

The overall approach adopted here was to use two separate codes – a flow solver and a structural solver, and to iterate between the two. This was achieved by iteratively computing (i) the flow field and pressure distribution resulting from a prescribed membrane geometry and (ii) the membrane shape resulting from a given pressure distribution. These two computations were performed iteratively until a stable steady-state solution was achieved.

### A. The Aerodynamic Model

The simulation of the flow field was done using the two-dimensional airfoil analysis tool, XFOIL [10]. For simplicity at this stage, only inviscid computations were performed, although viscous computations will be required for more accurate solutions, particularly at higher angles of attack where separation might be important. The membrane model must be translated into an appropriate airfoil model before its potential flow solution may be computed – XFOIL requires a single, continuous surface to be defined as a series of nodes. The membrane model's nodes are used as midpoints between top and bottom surface nodes. The membrane thickness,  $t$  may be used to specify the distance between the top and bottom surfaces, however with increasingly thin membranes, the analysis becomes increasingly singular. At thicknesses comparable to the previously conducted experiments (0.1% chord), the potential flow analysis fails to give meaningful results. It is also necessary to add smooth leading and trailing edge geometry to the XFOIL model to eliminate sharp corners. Elliptical leading and trailing edges were added to the XFOIL model, but their effects are neglected throughout the analysis. We found that a thickness of 1% chord, leading edge eccentricity of zero, and trailing edge eccentricity of 0.97 yield reasonable results from the XFOIL analysis.

The XFOIL analysis yields pressure coefficients at each of the surface nodes for the specified angle of attack  $\alpha$ . For each of the membrane nodes, the corresponding differential pressure, is calculated as the difference between top and bottom coefficients of pressure,  $\Delta C_p^i = C_{p^i \text{ bottom}} - C_{p^i \text{ top}}$ .  $\Delta C_p$  is defined such that a positive value corresponds to a positive chord-normal membrane deflection.

### B. The Structural Model

The airfoil is defined as a two-dimensional membrane with leading edge and trailing edge coordinates at  $(x, z) = (0,0)$  and  $(c,0)$  respectively. The membrane has a deflected profile,  $z(x)$ , approximated by  $N$  equally spaced nodes where the  $i$ th node has coordinates  $(x^i, z^i)$ . In physical terms, the membrane has an un-deflected chord,  $c$ , a thickness,  $t$ , an elastic modulus,  $E$ , and an un-stressed initial length,  $L_0$ . The membrane pre-strain,  $\varepsilon_0$ , is expressed as:

$$\varepsilon_0 = \frac{c - L_0}{L_0} \quad (1)$$

The deformed membrane length,  $L$ , is calculated as

$$L = \int_0^c \sqrt{1 + \left(\frac{dz}{dx}\right)^2} dx, \quad (2)$$

while the strain  $\varepsilon$ , is defined in terms of  $L$  and  $L_0$ :

$$\varepsilon = \frac{L - L_0}{L_0}. \quad (3)$$

The material behavior of the membrane is assumed to be linearly elastic, thus the tension,  $T$ , in the membrane may be expressed as

$$T = Et\varepsilon = Et \frac{L - L_0}{L_0} = Et \left( (\varepsilon_0 + 1) \cdot \left( \int_0^c \sqrt{1 + \left(\frac{dz}{dx}\right)^2} dx \right) - 1 \right). \quad (4)$$

The deflection of the membrane under differential pressure loading is behaves according to a Poisson equation:

$$\frac{d^2}{dx^2} z(x) + \frac{\Delta P}{T} = 0, \quad (5)$$

where  $T$  is the tension in the membrane's final configuration and will be independent of  $x$  due to the absence of skin friction in potential flow. Using the definition of  $T$ , (4), we can non-dimensionalize the above equation to obtain the governing differential equation:

$$\frac{d^2}{d(x/c)^2} \left(\frac{z}{c}\right) + \frac{\rho U^2 c}{2Et} \cdot \frac{\Delta C_p}{\varepsilon} = 0 \quad (6)$$

which is subject to homogeneous Dirichlet boundary conditions.

The problem is still underdetermined because the final configuration strain,  $\varepsilon$ , remains unknown. We enforce equilibrium between the chord-normal component of tension and the chord normal differential pressure load to fully constrain the problem. The chord-normal component of the tension forces at the leading and trailing edges,  $Tn$ , is expressed non-dimensionally as a function of  $\varepsilon$ :

$$Tn(\varepsilon) = \frac{2T(\varepsilon)}{\rho U^2 c} \left( \sin \left( \arctan \left( \frac{d}{d(x/c)} \left( \frac{z}{c} \right) \Big|_{\frac{x}{c}=0} \right) \right) + \sin \left( \arctan \left( - \frac{d}{d(x/c)} \left( \frac{z}{c} \right) \Big|_{\frac{x}{c}=1} \right) \right) \right), \quad (7)$$

and must balance the non-dimensional chord-normal aerodynamic load,  $F_n$ , which is calculated from  $\Delta C_p$

$$F_n = \int_0^1 \Delta C_p d(x/c). \quad (8)$$

The resulting equation,  $Tn(\varepsilon) - F_n = 0$ , fully determines the problem and ensures the structural forces balance the aerodynamic forces.

The differential pressure distribution is calculated discretely from the XFOIL analysis; we assume piecewise, linear behavior between nodes. The differential equation can now be solved exactly by a cubic spline [11]. Piecewise linear behavior of  $\Delta C_p$  suggests the use of trapezoidal integration to compute  $F_n$ . The choice of cubic spline interpolation is consistent with XFOIL's use of the cubic spline to interpolate between surface points. A custom MATLAB code solves the problem by applying the differential equation at each node and enforcing equilibrium.

### C. Equilibrium Configuration

We are interested in the equilibrium configuration of a membrane under specified flow conditions. We begin at  $0^\circ$  angle of attack ( $\alpha = 0^\circ$ ) with the known equilibrium solution  $z(x) = 0$  and calculate each equilibrium configuration, proceeding through the series of  $\alpha$  using the previous solution as the initial guess for the next iteration. At each  $\alpha$ , the membrane profile is updated from the calculated pressure distribution until a self-sustaining configuration is reached. The next membrane profile to be analyzed with XFOIL is a linear combination of the current computed membrane shape and the current membrane profile:

$$z_{next} = z_{current} + w(z_{computed} - z_{current}), \quad (9)$$

where  $w$  is a relaxation constant which is chosen to assist convergence. For our analysis, we used a relaxation parameter,  $w$ , equal to 0.5. This procedure is repeated until the airfoil shape converges as measured by the root-mean-squared change in the airfoil shape:

$$\sqrt{\frac{1}{N} \sum_{i=1}^N \left( \frac{z_{computed}^i - z_{last}^i}{\max(z_{computed})} \right)^2} < 5.0 \times 10^{-3} \quad (10)$$

The converged solution is then used as the initial guess for the iterative solution at the next angle of attack. Using this technique, a sequence of solutions was calculated for various values of  $E$  and  $\varepsilon_0$ .

## III. Simulation Results

The computer model presented here is an attempt to capture more detail in the behavior of compliant membrane wings than the previously suggested theory [9], but is by no means a complete model. It is important to remember that the flow being studied is the potential flow solution which fails to critical phenomenon such as flow separation and unsteady behavior which have been observed in the real flows. One must also remember that leading and trailing edge effects are ignored. The membrane deflection was solved using the Poisson equation which is valid for small deflection, yet we calculate deflections of over 30% chord length. Despite these mathematical shortcomings of this computer model, we find good agreement between our model and the previously proposed theory, an indication that the model is capturing the essential physics.

### A. Static Membrane Deflection

The simple theoretical model for membrane deflection suggested that the deflection of a membrane wing is a function of the pre-strain  $\varepsilon_0$ , and of the aerodynamic loading represented by a Weber number, [9]:

$$We = \frac{C_L \rho U^2 c}{2Et}. \quad (11)$$

Figure 1 illustrates the membrane maximum deflection as a function of Weber number, for a variety of pre-strain. The present results are compared with the predictions of the uniform loading model and the estimated operating range of *Cynopterus brachyotis*, which will be discussed later in this paper. The computed trend is very similar to the uniform loading theory, showing the same general trend for a fixed value of  $We$ , but the pre-strain in the computer model has a stronger effect on the  $We - z_{max}$  relationship than predicted by the theoretical model. In

particular, we see that the full computation predicts a lower deflection for a given value of pre-strain, however the family of curves generated at different values of  $\epsilon_0$  is preserved. Thus, when Song et al estimated the pre-strain in their experimental data required to fit the model, they likely overestimated the actual pre-strain (indeed the best-fit values of  $\epsilon_0$  that they reported were larger than they had initially estimated). We also see that for a specified *fixed* value of  $\epsilon_0$  the computed data fail to collapse onto a single curve, i.e.  $E - \alpha$  pairs which result in the same  $We$  do not produce the same  $z_{\max}$ . Given two membranes  $(E_1, \alpha_1)$  and  $(E_2, \alpha_2)$  subject to  $\epsilon_0$  and  $We$ , we take the first to be more compliant ( $E_1 < E_2$ ) and consistently find the first to have a larger  $z_{\max}$ , behavior which the uniform loading theory fails to predict.

The differential pressure distribution,  $\Delta C_p(x)$ , offers an explanation for these differences between the potential flow computations and the simple theory (Fig. 2). According to the uniform loading theory, the pressure is uniformly distributed along the chord length of the membrane, resulting, by definition in a parabolic membrane deflection profile. In contrast, however, the computed  $\Delta C_p(x)$  varies between membranes of different  $E$ ,  $\alpha$ , and  $\epsilon_0$ . At low modulus and pre-strain,  $\Delta C_p(x)$  takes a bell-shaped distribution, centered about mid-chord, more closely resembling the uniform pressure loading assumed in the simple model. As the membrane becomes increasingly stiff (either through increasing  $E$  or  $\epsilon_0$ ),  $\Delta C_p(x)$  increasingly resembles the pressure distribution observed on a more conventional rigid airfoil with the formation of a leading edge suction peak. This notion of the membrane becoming a rigid airfoil is supported by the migration of the center of pressure from mid-chord towards quarter-chord as predicted by thin airfoil theory [12]. Similarly, as the angle of attack increases,  $\Delta C_p(x)$  loses its symmetric bell structure. As the aerodynamic load shifts towards the leading edge, away from mid-chord, the resulting membrane deflection skews forward and decreases in amplitude.

## B. Lift Performance

In similar character to the observations from experiments of Song et al. [9], at low pre-strain, the equilibrium solution  $z(x) = 0$  is unstable and the membrane “snaps” into a cambered orientation once perturbed. This behavior allows a compliant membrane to maintain positive lift, even at slightly negative angles of attack. Some computed lift curves are shown in Fig. 3. The lift curves for the membranes under 0% and 5% pre-strain do not intersect the origin which demonstrates hysteresis is captured by this computer model. The computed lift curves were compared to thin airfoil theory and two equations from flexible sail theory associated with Thwaites [13] and Nielsen [14]. For a two-dimensional airfoil, the coefficient of lift is proportional to angle of attack:

$$C_L = 2\pi\alpha \quad (12)$$

while the sail theory has an additional term associated with the excess length:

$$C_L = 2\pi\alpha + A\sqrt{\frac{L-c}{c}} \quad (13)$$

with  $A = 6.36$  and  $A = 7.2784$  in Thwaites’ and Nielsen’s models [15], which are developed for small  $\alpha$ . Fig. 4 compares three different compliant membrane lift curves to these theories. Fig. 4 (a) shows that for 0% pre-strain, the computer model has excellent agreement with the sail theories even beyond  $\alpha = 20^\circ$ . As the pre-strain is increased in Fig. 4 (b,c) the membrane lift curve approaches thin airfoil theory.

## IV. In Vivo Methods

We now turn to in vivo measurements of membrane deflection from bats during flight. Previous descriptions of the experimental facility and setup are presented in more detail by Tian et al. [16] and by Riskin et al.[17], and are summarized here for convenience. The data were acquired from a number of wind tunnel flights of one individual of the lesser dog-faced fruit bat, *Cynopterus brachyotis*. These experiments were performed in the wind tunnel facility at the Harvard University Concord Field Station. This wind tunnel facility has a rectangular test section, with dimensions: 1.4 m length, 1.2 m width, 1.2 m height. For 97% of the wind tunnel test section the measured flow velocity is within 2.5% of the mean wind speed and the turbulence level of the tunnel is less than 1.28% [18].

The bat was marked with an array of 54 markers distributed over the left wing as shown in Figure 5. Self-adhesive retroreflective markers (3M Scotchlite) were placed on the skin membrane while the skeletal members and body reference points were marked with a non-toxic acrylic white paint. The marked bat was then flown in the wind tunnel and the three-dimensional motion of the markers was recorded at a frame rate of 1000Hz ( $\Delta t=1$  millisecond) through the use of three high-speed video cameras (Photron PCI-1024). A fraction of the test section was calibrated using the Direct Linear Transformation method (DLT) [19], which can determine the 3-dimensional coordinates of a marker in the calibrated volume if the marker is seen in at least two camera views. The time-varying locations of these markers were then digitized and reconstructed 3-dimensionally via DLT using a custom MATLAB program.

The surface of the wing was discretized into triangular elements formed by the connective edges between the markers, as shown in Fig. 2. For the surface area analysis, the wing was divided into 5 regions according to the natural subdivision of the wing membrane between bony members. The plagiopatagium is further subdivided due to the size of the plagiopatagium as compared to the other regions; more detailed analyses are possible by interrogating smaller groupings of elements or even individual elements.

Each triangular element can be represented by two vectors with the same origin. If these two vectors are denoted by  $\mathbf{u}$  and  $\mathbf{v}$ , then the area of the triangle formed by these two vectors is

$$A = \frac{1}{2} |\mathbf{u} \times \mathbf{v}|. \quad (14)$$

The representation of a three-dimensionally curved surface with flat two-dimensional mesh elements leads to an underestimation of the true area of the membrane. However, the dense distribution of markers in this experiment keeps this source of measurement error small.

The variation of the surface area of each of these membrane regions is expressed as the surface area normalized by a reference area,  $A_0$ . The mid-downstroke area was selected as this reference area,  $A_0$ , due to the consistency of this value across wingbeats and the decreased reliance on interpolation during this portion of the wingbeat. In addition, previous work which utilizes a quasi-steady model for the generation of aerodynamic forces assumes that the mid-downstroke wing geometry is representative of the wing shape for analysis [20, 21].

## V. In Vivo Results

In flight, the bat's wings undergo significant deformation due in part to the large number of articulations in the wing which allow the animal to actively make quite dramatic changes to the wing shape [22]. In addition, the wing is composed of a compliant skin membrane which stretches and recoils due to the presence and absence of aerodynamic forces respectively. This interplay between the aerodynamic force generation and the membrane geometry can have significant effects on the overall aerodynamic performance of the compliant wing [9]. We present detailed kinematic data which demonstrate the high degree of variation in a bat's wings during flight. These data underscore the importance of skin compliancy to the aerodynamic performance of bats.

We present an illustrative case ( $U = 4.1$  m/s) in Fig. 5 where the membrane exhibits behavior consistent with the other forward flight speeds considered ( $U = 2.6$  and  $6.6$  m/s, not shown in the current manuscript). The surface area of the plagiopatagium nearly doubles during the wingbeat cycle with the maximum area reached at the bottom of the downstroke, or lower reversal point. In contrast, the surface area of the propatagium and hand wing portions of the membrane show no more than a 40% relative change in the surface over the wingbeat cycle. The increase in surface area of the propatagium is relatively small, only expanding by less than 10% during the portion of the wingbeat between mid-downstroke and the lower reversal point. Similar to the deformation behavior of the propatagium, the two sections of dactylopatagium that comprise the handwing also exhibit small values of membrane expansion from mid-downstroke to the lower reversal point. In fact, the value of relative surface areas of the propatagium and dactylopatagia plateau during this portion of the wingbeat suggesting that the wing's skeletal frame has reached full extension near mid-downstroke. Although not shown here, similar trends in the surface area variation was also observed at both the lower and higher speeds tested. Indeed, the overall change in wing area did not change appreciably as a function of speed, suggesting that the animal has a preferred compliance and uses other mechanisms (such as angle of attack, flapping amplitude and frequency, etc) to moderate the lift force as the dynamic pressure changes.

The deformation behavior of the plagiopatagium and the other regions (propatagium and dactylopatagium) of the wing differed. As seen in Fig. 6, the plagiopatagium continues to expand throughout the entire downstroke and consistently reaches the maximum surface area at the bottom of the downstroke while the propatagium and dactylopatagia reach a maximum near mid-downstroke and maintain this value until the beginning of the upstroke. This plateau may be due to the strong dependence of the skeletal framework of the wing and the shape of these regions of wing membrane. The triangular propatagium is bordered on two sides by the radius and humerus, the stiffest bones in the wing's skeletal structure therefore the surface area of the propatagium is governed primarily by the elbow joint angle. Likewise, the triangular regions of wing membrane which comprise the dactylopatagia are also constrained by the bordering digits. Therefore, the plateau in the surface area for the propatagium and dactylopatagia indicates that the expansion of the membrane due to the extension of the arm and digits concludes by mid-downstroke while the plagiopatagium continues to expand until the end of the wingbeat. The further "ballooning" of the plagiopatagium suggests that the aerodynamic loading is the primary mechanism for the further stretching of the arm wing membrane. This aeroelastic response of the plagiopatagium may allow the animal to generate high values of lift at the end of the downstroke and into the beginning of the upstroke due to the cambering

of the wing due to the further deflection of the wing. The enhanced lift due to increased camber would be important to offset a decrease in lift as the wing begins to fold on the upstroke.

## VI. Discussion and Conclusions

The two approaches presented here – computational and experimental – complement each other in interesting ways. The computational results illustrate how the membrane behaves subject to real aerodynamic forces, unlike the simple uniform loading case originally considered by Song et al [9]. However, the differences between these two approaches are surprisingly small. The general relationship between the membrane deflection and Weber number captured by the simple model is preserved in the XFOIL calculation despite an imperfect application of the Weber number scaling for the simple model (specifically, the angle of attack and dynamic pressure are not equivalent means for generating membrane loading). It is, again, surprisingly robust at least as a first approximation for the wing behavior. A key difference between the simple and improved model is that the role pretension plays in this computer model is more profound than in the simplified theory. The pretension prevents the membrane from cambering outward and the differential pressure distribution is shifted closer to the leading edge. The forward shift in pressure concentration results in a center of pressure forward of mid-chord where the resulting membrane deformation is reduced. The result is a smaller maximum camber than predicted by the simple theory which assumes an evenly distributed pressure. It is important to remember that the modeled flow is inviscid and fails to predict flow separation which is likely to occur on highly cambered membranes and at large angles of attack. Nevertheless, this computer model of the compliant membrane captures the same qualities predicted by the simple theory while giving insight to the importance the pressure distribution plays in cambered shape and how it is affected by membrane pretension.

The results of the in vivo membrane deformation measurements are dramatic in that they demonstrate the extreme compliance of the bat wings during flight and the dynamic shape morphing of the animal's wings in flight. Unlike a bird or insect's wings, we show that a bat's wing can undergo a change in area of approximately 100% over a wingbeat cycle. However, despite the extraordinary variation in the surface area of the wing, which has strong implications for generation of aerodynamic forces, the maximum camber,  $z/c$ , of the wing hovers about 10% of the chord length, as seen in Fig. 7, during what we are assuming to be the aerodynamically active portion of the wingbeat (from 25% of the downstroke to 25% of the upstroke). In Fig 1., we relate the airfoil shape observed in the flight experiments with those seen in the computational model and observe that according to the computational model that the animal can significantly change the camber of the wing through slight changes of the membrane pre-strain. The fact that the stretching behavior of the membrane does not increase with speed and the relatively small range of camber values suggest that the animal restricts excess deflection at higher speeds (and higher dynamic pressure) by either decreasing  $C_L$  or by increasing the pre-tension (by means of muscles in the wing membrane), or some combination of the two. Further computational studies which include the implementation of a viscous fluid model and more in depth examination of the correlation between the wing shapes found in vivo and the aerodynamic forces generated are needed to unpack the exciting potential of an active control mechanism (the aforementioned muscles) embedded in the wing membrane.

## Acknowledgements

This work was supported by the Air Force Office of Scientific Research, monitored by Drs Rhett Jeffries and Willard Larkin.

## References

- <sup>1</sup>T. J. Mueller and J. D. DeLaurier, "Aerodynamics of Small Vehicles," *Annual Review of Fluid Mechanics*, Vol. 35, 2003, pp. 89-111
- <sup>2</sup>E. V. Laitone, "Wind Tunnel Tests of Wings at Reynolds Numbers Below 70 000," *Experiments in Fluids*, Vol. 23, 1997, pp. 405-409
- <sup>3</sup>P. Rojratsirikul, Z. Wang and I.Gursul, "Unsteady Aerodynamics of Membrane Airfoils," *AIAA Aerospace Sciences Meeting*, AIAA Paper 2008-613, 2008
- <sup>4</sup>R. Gordnier, "High Fidelity Computational Simulation of a Membrane Wing Airfoil," *AIAA Aerospace Sciences Meeting*, AIAA Paper 2008-614, 2008
- <sup>5</sup>W. Shyy, M. Berg and D. Ljungqvist, "Flapping and Flexible Wings for Biological and Micro Air Vehicles," *Progress in Aerospace Sciences*, Vol. 35, No. 5, 1999, pp. 455-505
- <sup>6</sup>W. Shyy, F. Klevebring, M. Nilsson, J. Sloan, B. Carroll and C. Fuentes, "Rigid and Flexible Low Reynolds Number Airfoils," *Journal of Aircraft*, Vol. 36, No. 3, 1999, pp. 523-529

- <sup>7</sup>Y. S. Lian, W. Shyy, D. Viieru and B. N. Zhang, "Membrane Wing Aerodynamics for Micro Air Vehicles," *Progress in Aerospace Sciences*, Vol. 39, No. 6-7, 2003, pp. 425-465
- <sup>8</sup>Y. S. Lian and W. Shyy, "Numerical Simulations of Membrane Wing Aerodynamics for Micro Air Vehicle Applications," *Journal of Aircraft*, Vol. 42, No. 4, 2005, pp. 865-873
- <sup>9</sup>A. Song, X. Tian, E. Israeli, R. Galvao, K. Bishop, S. Swartz and K. Breuer, "Aeromechanics of Membrane Wings with Implications for Animal Flight," *ALAA Journal*, 2008, (in press)
- <sup>10</sup>M. Drela, "Xfoil: An Analysis and Design System for Low Reynolds Number Airfoils.," *Low Reynolds Number Aerodynamics. Lecture Notes in Engineering, Vol 54.*, edited by T. J. Mueller, Springer Verlag, 1989
- <sup>11</sup>P. Moin, *Fundamentals of Engineering Numerical Analysis*, Cambridge University Press, Cambridge, United Kingdom, 2001
- <sup>12</sup>J. D. Anderson, "Fundamentals of Aerodynamics," Third ed., McGraw-Hill, 2001
- <sup>13</sup>B. Thwaites, "The Aerodynamics Theory of Sails. I. Two-Dimensional Sails," *Proc. Roy. Soc. Lond. A*, Vol. 261, 1961, pp. 402-422
- <sup>14</sup>J. N. Nielsen, "Theory of Flexible Aerodynamic Surfaces.," *Trans. ASME: J. Appl. Mech.*, Vol. 30, 1963 pp. 435-442
- <sup>15</sup>O. Lorillu, R. Weber and J. Hureau, "Numerical and Experimental Analysis of Two-Dimensional Separated Flows over a Flexible Sail," *Journal of Fluid Mechanics*, Vol. 466, 2002, pp. 319-341
- <sup>16</sup>X. Tian, J. Iriarte-Diaz, K. Middleton, R. Galvao, E. Israeli, A. Roemer, A. Sullivan, A. Song, S. Swartz and K. Breuer, "Direct Measurements of the Kinematics and Dynamics of Bat Flight," *Bioinspiration & Biomimetics*, Vol. 1, No. 4, 2006, pp. S10-S18
- <sup>17</sup>D. K. Riskin, D. J. Willis, J. Iriarte-Diaz, T. L. Hedrick, M. Kostandov, J. Chen, D. H. Laidlaw, K. S. Breuer and S. M. Swartz, "Quantifying the Complexity of Bat Wing Kinematics," *Journal of Theoretical Biology*, 2008, (in press)
- <sup>18</sup>T. L. Hedrick, B. W. Tobalske and A. A. Biewener, "Estimates of Circulation and Gait Change Based on a Three-Dimensional Kinematic Analysis of Flight in Cockatiels (*Nymphicus Hollandicus*) and Ringed Turtle-Doves (*Streptopelia risoria*)," *The Journal of Experimental Biology*, Vol. 205, 2002, pp. 1389-1409
- <sup>19</sup>H. Hatze, "High-Precision Three-Dimensional Photogrammetric Calibration and Object Space Reconstruction Using a Modified DLT-Approach," *J. Biomechanics*, Vol. 21, 1988, pp. 533-538.
- <sup>20</sup>U. M. Norberg, *Vertebrate Flight: Mechanics, Physiology, Morphology, Ecology and Evolution*, Springer-Verlag, Berlin, 1990
- <sup>21</sup>P. Watts, E. J. Mitchell and S. M. Swartz, "A Computational Model for Estimating the Mechanics of Horizontal Flapping Flight in Bats: Model Description and Validation," *The Journal of Experimental Biology*, Vol. 204, No. 16, 2001, pp. 2873-2898
- <sup>22</sup>S. M. Swartz, K. L. Bishop and M. F. Ismael-Aguirre, "Dynamic Complexity of Wing Form in Bats: Implications for Flight Performance," *Functional and Evolutionary Ecology of Bats*, edited by Z. Akbar, G. McCracken and T. H. L. Kunz, Oxford, New York, 2005

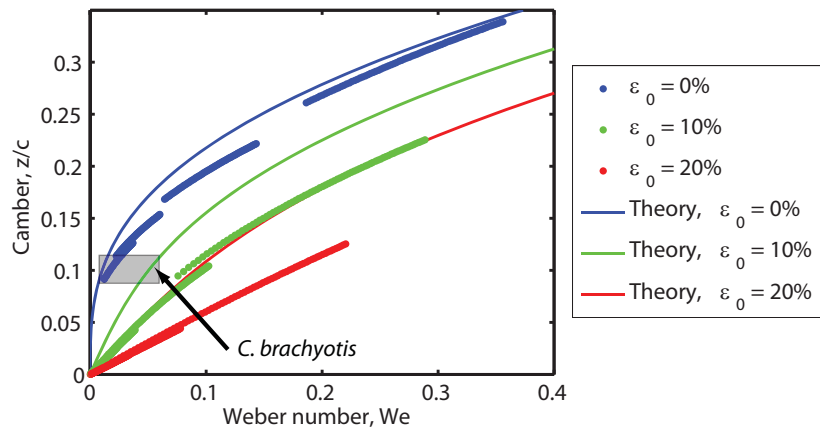


**Figure 1. Maximum camber as a function of aerodynamic loading.** The maximum camber calculated from the inviscid flow model is plotted as a function of the Weber number,  $We = C_L \rho U^2 c / (2Et)$ , and compared with the simple theoretical model. The calculated data were obtained by solving the membrane model with specified moduli and pre-strains through increasing of angles of attack. The different pre-strain sets plotted are comprised of solution sets of four different elastic moduli ( $2Et/(\rho U^2 c) = 15.5, 31.0, 62.0, \text{ and } 93.0$ ). At a specified pre-strain, there are many combinations of angle of attack and modulus which give the same Weber number, yet they result slightly different camber values. The shaded rectangular region is the estimated operating range of the *Cynopterus brachyotis* during the downstroke portion of the wingbeat. This suggests that the animal may be able to make significant changes in the camber of the wing through slight adjustment of the membrane pre-strain using thin, chordwise muscles present in the membrane.

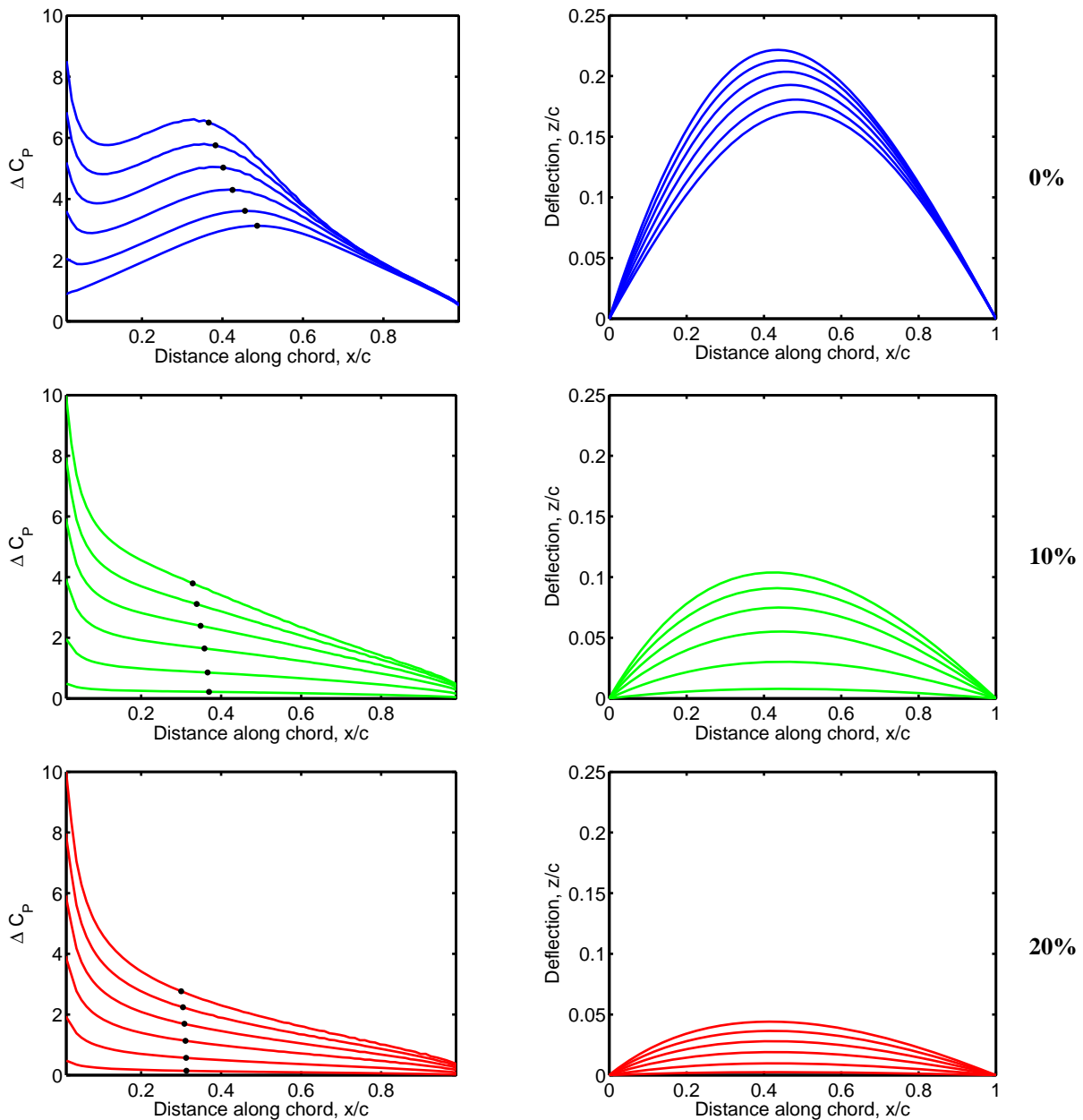


**Figure 2. Pressure distributions and membrane deflection.** The computed differential pressure distributions are plotted for three pre-strains (Blue: 0%, Green: 10%, and Red: 20%) over a range of angles of attack (1-20°) resulting from potential flow computations. The solid symbol represents the location of the center of pressure. The 0% pre-strain model has the most symmetric pressure distribution which is most similar to the uniform-loading theory. With increasing pre-strain, the pressure distribution approaches the behavior predicted by thin airfoil theory for rigid airfoils. The potential flow solution remains fully attached over the membrane, resulting greater lift than would be expected from a viscous flow. ( $2Et/(\rho U^2 c) = 31.0$ ).

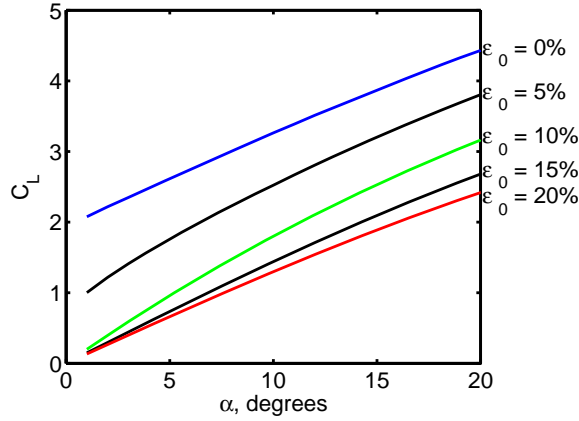


**Figure 3. Inviscid model lift performance.** The lift generated by membranes of varying pre-strain are compared over a range of angles of attack. Low pre-strain models exhibit hysteresis about zero angle of attack and do not approach zero lift as  $\alpha$  decreases. The 0% and 5% pre-strain models are in unsteady equilibrium at zero angle of attack. As the pre-strain is increased, the membrane becomes more like a rigid airfoil and the zero angle of attack becomes a steady equilibrium. ( $2Et/(\rho U^2 c) = 31.0$ )

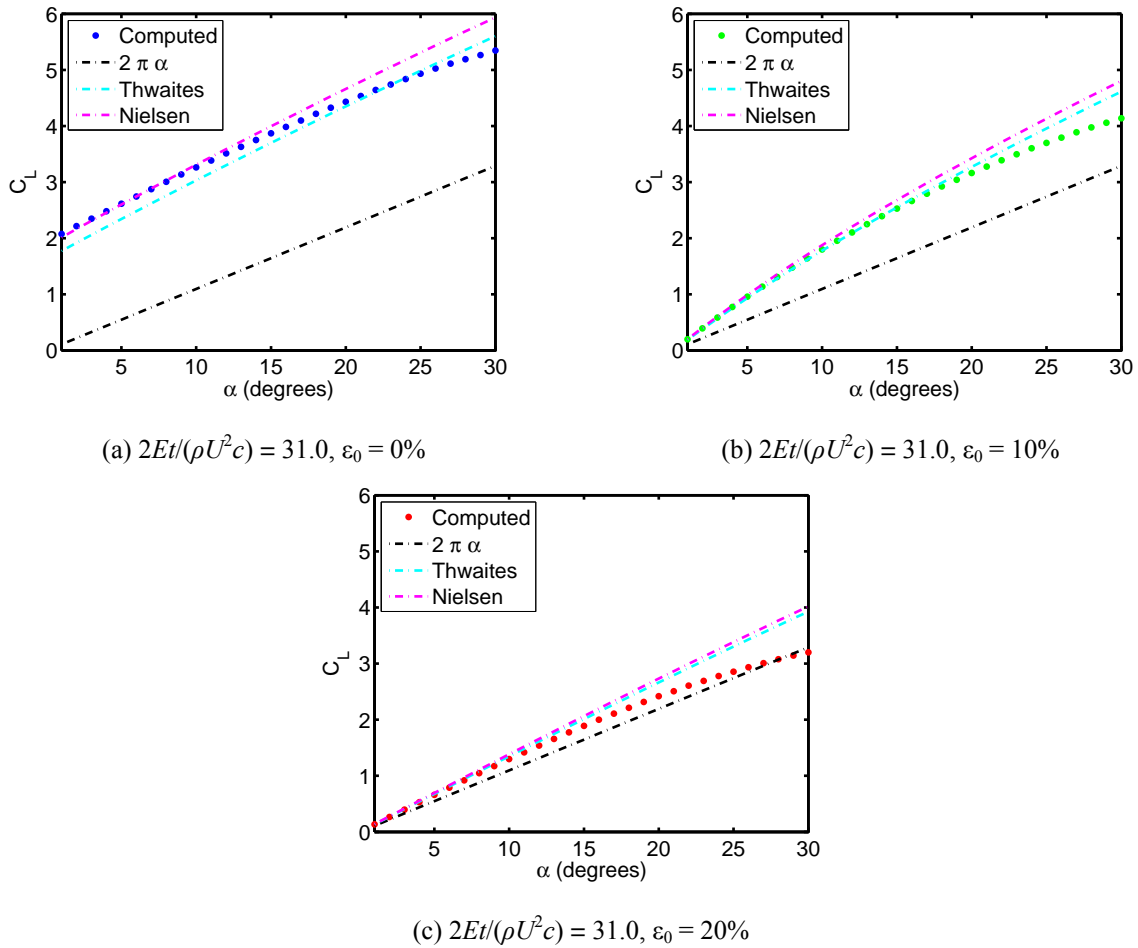


**Figure 4. Computed lift performance versus theory.** The computed lift curves agree well with lift equations from Thwaites and Nielsen for a sail. As the membrane pretension increases, the membrane behaves essentially as a rigid airfoil.

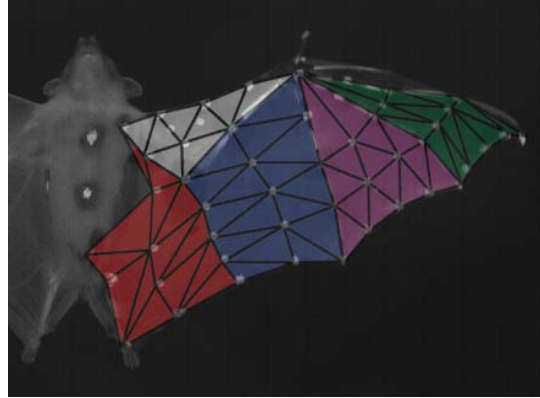


**Figure 5. Analysis mesh construction from markers.** The bat was marked with an array of 54 markers distributed over the left wing as shown above. The time-varying locations of these markers were then digitized and reconstructed 3-dimensionally via DLT using a custom MATLAB program. The surface of the wing was discretized into triangular elements formed by the connective edges between the markers, as shown above. For this analysis, the wing was divided into 5 regions indicated by the colored patches according to the natural subdivision of the wing membrane between bony members. The plagiopatagium is further subdivided into proximal and distal section due to the size of the plagiopatagium as compared to the other regions. The regions considered for analysis are the proximal plagiopatagium (red), distal plagiopatagium (blue), propatagium (white), dactylopatagium (digits IV-V) (magenta), and dactylopatagium (digits III-IV) (green).

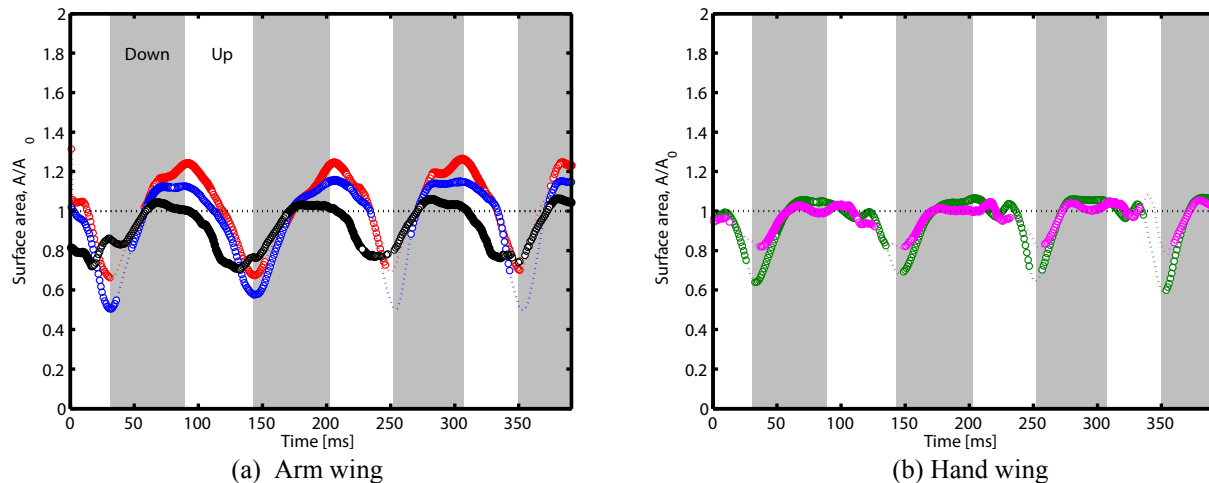


**Figure 6. Wing surface area.** The variation of a normalized surface area with respect to time is shown for a representative case ( $U=4.1$  m/s). The change in the regional surface area relative to the mid-downstroke surface area of each of the wing regions are plotted against time. For these data, it is impossible to define an original, relaxed state to serve as a reference for the surface area variation, therefore the mid-downstroke area served as the normalizing value for the relative surface area change. (Left) Arm wing – (●) plagiopatagium (proximal), (●) plagiopatagium (distal), (●) propatagium. (Right) Hand wing – (●) dactylopatagium (digits III-IV), (●) dactylopatagium (digits IV-V). Filled-in symbols, (e.g., ●): 100% of markers in view. Open symbols (e.g., ○): more than 50% of markers in view. Dotted lines (e.g., - -): Less than 50% of markers in view.

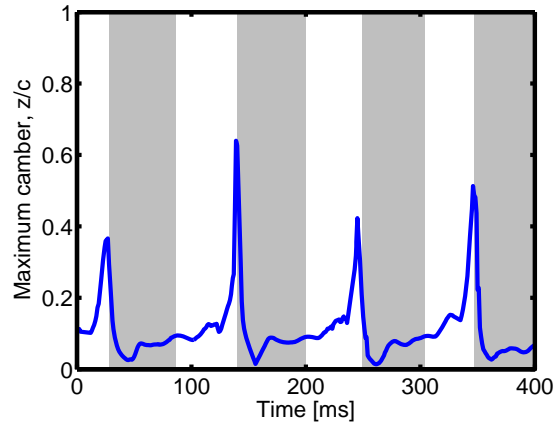


**Figure 7. Variation of camber during the wingbeat cycle.** *The variation of the maximum camber of the membrane airfoil shape with respect to time is shown for a representative case ( $U=4.1$  m/s). Over a significant portion of the wingbeat cycle (arguably the portion during which most of the aerodynamic forces are generated by the wing), the camber is relatively constant and hovers around the value of 10% of the chord length. The spikes in the value of the camber near the top of the upstroke are to be expected since wing will fold significantly during this portion of the wingbeat.*